

See discussions, stats, and author profiles for this publication at: <https://www.researchgate.net/publication/221977370>

# Programmable Light-Controlled Shape Changes in Layered Polymer Nanocomposites

ARTICLE in ACS NANO · MARCH 2012

Impact Factor: 12.88 · DOI: 10.1021/nn204938j · Source: PubMed

CITATIONS

31

READS

76

## 4 AUTHORS:



Zhichen Zhu

Stevens Institute of Technology

10 PUBLICATIONS 269 CITATIONS

SEE PROFILE



Erkan Senses

National Institute of Standards and Technol...

18 PUBLICATIONS 61 CITATIONS

SEE PROFILE



Pinar Akcora

Stevens Institute of Technology

50 PUBLICATIONS 613 CITATIONS

SEE PROFILE



Svetlana Sukhishvili

Stevens Institute of Technology

134 PUBLICATIONS 4,815 CITATIONS

SEE PROFILE

# Programmable Light-Controlled Shape Changes in Layered Polymer Nanocomposites

Zhichen Zhu,<sup>†</sup> Erkan Senses,<sup>‡</sup> Pinar Akcora,<sup>‡</sup> and Svetlana A. Sukhishvili<sup>†,\*</sup>

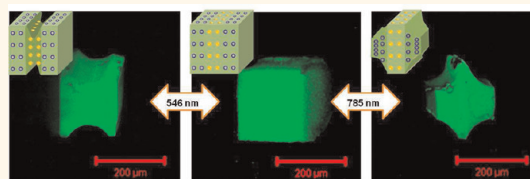
<sup>†</sup>Department of Chemistry, Chemical Biology and Biomedical Engineering, Stevens Institute of Technology, Castle Point on Hudson, Hoboken, New Jersey 07030, United States and <sup>‡</sup>Department of Chemical Engineering and Materials Science, Stevens Institute of Technology, Castle Point on Hudson, Hoboken, New Jersey 07030, United States

The plant and animal worlds are replete with examples of complex shape transformations including leaf and skin wrinkling, goose bumps, and octopus adaptive-camouflage skin shape changes. Mimicking environmental responsiveness of living creatures has been an attractive, yet challenging, topic of research for decades. Stimuli-responsive synthetic polymers capable of changing their conformation in response to multiple stimuli (pH, temperature, ionic strength, and others) are highly suitable for building artificial biomimetic materials and have been used to generate a variety of smart polymer films and nano- and microparticles.<sup>1,2</sup> These systems have been used to control protein<sup>3</sup> and cellular<sup>4</sup> adhesion, as well as for applications in sensing and actuation,<sup>5</sup> including muscle-mimicking materials.<sup>6</sup>

Among various environmental stimuli applied to induce materials response, light is especially attractive, as it allows for remote actuation of material properties, without the need to change the surrounding environment. A number of studies have focused on relatively simple geometric variations with nonaqueous polymers or polymer nanocomposites. Light-induced bending of liquid-crystalline polymers caused by *trans*–*cis* isomerization of azobenzene chromophores<sup>7–9</sup> and remote actuation of polymer-carbon nanotube composites using infrared radiation<sup>10,11</sup> have both been explored.

Of specific interest is actuation in an aqueous environment, an avenue leading to applications of shape-changing materials in biomedicine. Combining temperature-responsive, water-soluble polymers with metal nanoparticles, for example, allows the use of heat produced as a result of light absorption and scattering at plasmonic nanostructures to induce hydration/

## ABSTRACT



We present soft, layered nanocomposites that exhibit controlled swelling anisotropy and spatially specific shape reconfigurations in response to light irradiation. The use of gold nanoparticles grafted with a temperature-responsive polymer (poly(*N*-isopropylacrylamide), PNIPAM) with layer-by-layer (LbL) assembly allowed placement of plasmonic structures within specific regions in the film, while exposure to light caused localized material deswelling by a photothermal mechanism. By layering PNIPAM-grafted gold nanoparticles in between nonresponsive polymer stacks, we have achieved zero Poisson's ratio materials that exhibit reversible, light-induced unidirectional shape changes. In addition, we report rheological properties of these LbL assemblies in their equilibrium swollen states. Moreover, incorporation of dissimilar plasmonic nanostructures (solid gold nanoparticles and nanoshells) within different material strata enabled controlled shrinkage of specific regions of hydrogels at specific excitation wavelengths. The approach is applicable to a wide range of metal nanoparticles and temperature-responsive polymers and affords many advanced build-in options useful in optically manipulated functional devices, including precise control of plasmonic layer thickness, tunability of shape variations to the excitation wavelength, and programmable spatial control of optical response.

**KEYWORDS:** nanocomposites · light-responsive materials · soft actuators · shape-changing materials · zero Poisson's ratio · metal nanoparticles · photothermal effect · poly(*N*-isopropylacrylamide) · rheology

collapse of temperature-responsive polymer chains and volume changes in the material. This phenomenon, called the photothermal effect, has been used to remotely control nanoparticle self-assembly,<sup>12</sup> to trigger release of bioactive molecules from dispersed nanoparticle–polymer structures<sup>13–15</sup> or nanocomposite materials,<sup>16</sup> or to remotely control microfluidic valves made of nanocomposite hydrogel.<sup>17</sup> So far,

\* Address correspondence to ssukhish@stevens.edu.

Received for review December 17, 2011 and accepted March 27, 2012.

Published online March 27, 2012  
10.1021/nn204938j

© 2012 American Chemical Society

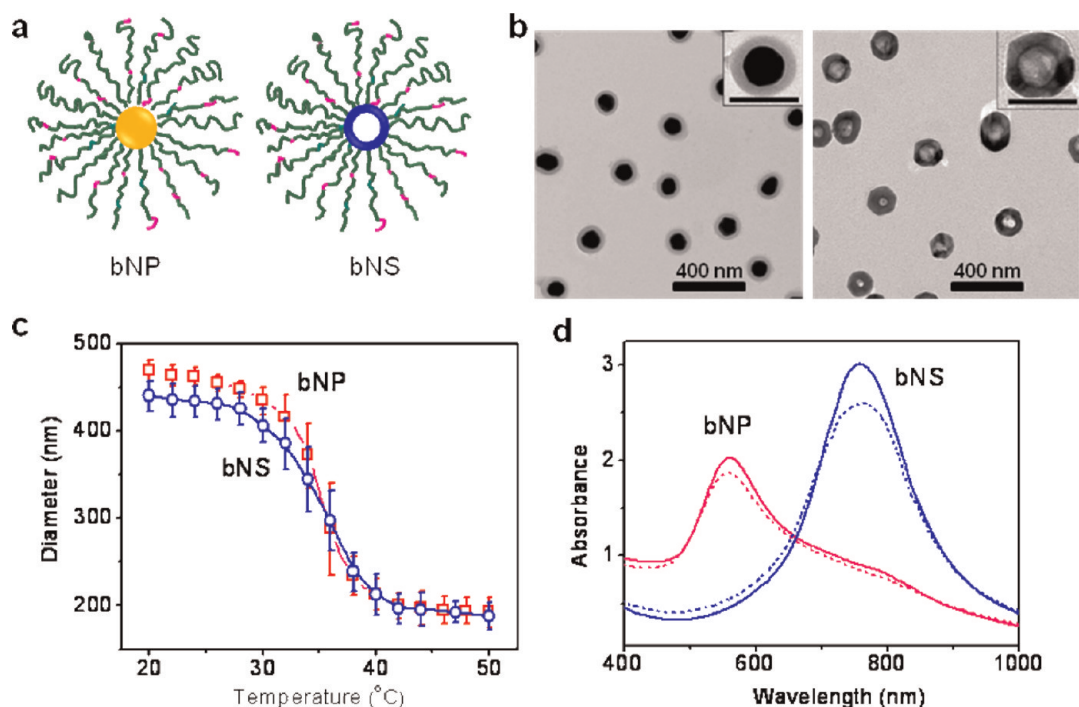


**Figure 1.** Gold nanoparticles and nanoshells modified with polymer brushes. (a) Schematic representation of a gold nanoparticle (left) and a gold nanoshell (right) modified with a random copolymer with 98:2 molar ratio of NIPAM (green) and DMA (red) units, denoted as bNP and bNS, respectively. (b) TEM images of bNPs and bNSs dried from buffer solutions at pH 3.0. The scale bar in the insets is 150 nm. Metallic NPs and NSs had diameters of  $70 \pm 10$  and  $65 \pm 6$  nm, respectively, and the nanoshell thickness was  $\sim 4$  nm (determined by TEM, Figure S1). (c) Hydrodynamic diameters of bNP and bNS in 1% (by weight) solutions at pH 3.0 versus temperature, determined by dynamic light scattering. Error bars represent the standard deviation of the mean diameter averaged over three measurements. (d) UV-vis absorption spectra in the same solutions at 20 °C (dotted lines) and 40 °C (solid lines).

however, this approach has been restricted either to individually dispersed gold nanoparticles<sup>13–19</sup> or to hydrogels of temperature-responsive polymers containing randomly distributed metal nanostructures.<sup>16,17,20–25</sup> Regardless of the type of stimuli applied to induce the response, realization of complex shape changes with synthetic materials has remained a challenge.

Precise control of spatial arrangements of plasmonic nanostructures within environmentally responsive polymer matrices could meet essential needs in modern tissue engineering, biomedicine, and microfluidics, supplying new nanostructured materials that exhibit remotely triggered, diverse, reversible shape changes. Importantly, shape changes of such materials can be preprogrammed at the step of material assembly, and multiple shapes can be realized with the same constructs by varying the excitation wavelength. Here, we apply the layer-by-layer (LbL) technique<sup>26–31</sup> to assemble plasmonic nanostructures covered with temperature-responsive brushes,<sup>5,32–34</sup> within multilayer films, and show that swelling of such assemblies is highly sensitive to temperature variations and/or illumination with light at wavelengths resonant to absorption and scattering of assembled plasmonic nanostructures. We demonstrate that layering of light-responsive, polymer-decorated nanoparticles/nanoshells in between nonresponsive polymer layers

leads to anisotropy of swelling, while incorporation of various plasmonic nanostructures within different film strata allows for complex shape architectures. Unlike previously reported glassy assemblies of bare nanoparticles and polyelectrolytes, which irreversibly ruptured as a result of radiation-induced extreme heat generation,<sup>35–37</sup> our nanocomposites are soft and exhibit complex, fully reversible shape changes. This is enabled by the use of nanoparticles modified with temperature-responsive polymer brushes, which collapse reversibly when local heating caused by light absorption raises the local temperature by only several degrees above ambient.

## RESULTS AND DISCUSSION

Two types of polymer-grafted gold nanostructures were used as LbL film building blocks (Figure 1). Metal cores were either solid gold nanoparticles (NPs) or gold nanoshells (NSs) (Figure S1 in the Supporting Information). Solid NPs with diameter  $70 \pm 10$  nm were synthesized according to the procedures adapted from Jana *et al.*,<sup>38</sup> while NSs with  $65 \pm 6$  nm external diameter and  $\sim 4$  nm shell thickness were synthesized *via* galvanic replacement reaction using cobalt nanoparticle templates and gold tetrachloroauric acid ( $\text{HAuCl}_4$ ).<sup>39</sup> A temperature-responsive random copolymer of *N*-isopropylacrylamide, NIPAM, (green), and

2-(dimethylamino)ethyl methacrylate, DMA (red), units was “grafted from” gold cores (Figure 1a) using atom transfer radical polymerization. Gold nanoparticles and gold nanoshells modified with the copolymer brushes are denoted as bNP and bNS, respectively. Figure 1b shows that polymer brush coatings at the metal cores had dry thicknesses of  $\sim 35$  and  $\sim 40$  nm for bNPs and bNSs, respectively. Molecular weights, chemical compositions, and grafting densities of polymer chains were determined after cleaving of grafted chains with iodine.<sup>40</sup> The molecular weights of grafted chains, determined by gel permeation chromatography (GPC), were 175 and 197 kDa for bNPs and bNSs, respectively (Figure S2, a). The molar ratio of NIPAM to DMA units calculated from  $^1\text{H}$  NMR spectra (see Methods and Figure S2, b) was 98:2. A small number (2%) of DMA units promoted colloidal stability of polymer-modified NPs and assisted in their assembly with a polyanion. Chain grafting densities were also determined from a combination of GPC and thermogravimetric analysis (TGA) (Figures S2 and S3) and were found to be 0.18 and 0.15 chains/nm<sup>2</sup> for bNPs and bNSs, respectively. An example of calculation of copolymer grafting density for the case of bNPs is given in the Supporting Information.

PNIPAM chains are temperature-responsive; that is, they dehydrate and collapse when solution temperature is raised above  $\sim 32$  °C (lower critical solution temperature, LCST, behavior).<sup>41,42</sup> Figure 1c shows that inclusion of a small percentage of cationic units did not significantly affect PNIPAM's LCST (bNPs and bNSs deswelled in the range of temperatures from 32 to 40 °C). At the same time, nanoparticle aggregation at temperatures above LCST was avoided by introducing cationic DMA units ( $\text{p}K_{\text{a}}$  6.7) to provide interparticle repulsions. Estimated from dynamic light scattering results in Figure 1c, the swollen polymer brush thicknesses were  $\sim 195$  nm at 20 °C and  $\sim 60$  nm at 40 °C for bNPs and  $\sim 185$  nm at 20 °C and  $\sim 60$  nm at 40 °C for bNSs. These values correspond to swelling ratios  $\lambda$  (defined as the ratio of wet to dry brush thicknesses) of 5.5 and 1.7 for bNPs and of 4.6 and 1.6 for bNSs at 20 and 40 °C, respectively. These amplitudes of swelling/deswelling transitions for grafted temperature-responsive chains are consistent with earlier observations with relatively dense temperature-responsive brushes.<sup>43</sup> Incomplete deswelling at high temperatures reflects the presence of a significant amount (at least 40% of dry weight) of water in thermally collapsed PNIPAM chains.<sup>44</sup> Interestingly, when allowed to adsorb at the surface of a silicon wafer precoated with a monolayer of PMAA (adsorbed from 0.2 mg/mL solutions at pH 3) in order to provide the substrate with centers of hydrogen bonding, bNP particles showed a distinct change in their shape from spherical to hat-like geometry in response to an increase in temperature above PNIPAM's LCST (Figure S4).

We then aimed to assemble bNPs and bNSs within multilayer films and to explore stimuli response behavior of the assembled materials. Figure 1d shows that bNP and bNS building blocks absorbed light in distinct spectral regions (with absorption maxima at 550 and 760 nm for bNP and bNS). Indeed, tuning of the surface plasmon resonance band in a wide spectral region is commonly achieved through variation of metal nanostructure shape and size.<sup>45</sup> The bNP and bNS building blocks were then assembled within LbL films using a spin-assisted technique<sup>46–48</sup> with poly(methacrylic acid) homopolymer, PMAA ( $M_{\text{w}}$  = 150 kDa), at pH 3. Assembly at this low pH value allowed NIPAM units in bNP or bNS coronas to form hydrogen bonds with protonated PMAA units.<sup>49</sup> When bNPs or bNSs are assembled in alternation with a PMAA homopolymer (Figure 2a,b, left), the films are called layered bNP or bNS assemblies and denoted as bNP<sub>*n*</sub> or bNS<sub>*n*</sub>, respectively, where *n* is the number of bNP(or bNS)–PMAA repeat bilayers. Layered films with two types of nanoparticles were also assembled having both bNP and bNS assembled strata (Figure 2a,b, middle). Finally, hybrid layered bNP films were constructed, consisting of nonswellable all-polymer PNIPAM/PMAA polymer strata of PNIPAM homopolymer ( $M_{\text{w}}$  = 300 kDa) and PMAA (abbreviated as “pol” strata) deposited between swellable bNP layers (Figure 2a,b, right). These films are abbreviated as [bNP<sub>1</sub>–pol<sub>*n*</sub>]<sub>*m*</sub> where *n* is the number of PNIPAM/PMAA bilayers deposited between bNP layers and *m* is the number of bNP<sub>1</sub>–pol<sub>*n*</sub> repeated motifs. All film types obtained by spin-assisted layer-by-layer deposition showed strong nanoparticle stratification (Figure 2b). SEM images of films of other architectures are shown in Figure S5. Figure 2c illustrates that dry film thicknesses deposited within each bNP or bNS bilayer ( $\sim 106$  and  $\sim 115$  nm) were comparable with diameters of dry unassembled bNP and bNS nanoparticles (120 and 130 nm, respectively, Figure 1c). This indicates almost complete monolayer coverage during adsorption of bNPs or bNSs within films. Assembled films were temperature responsive and could be delaminated from the substrate to form a free-standing film<sup>31,50</sup> by applying several cycles of temperature variations above and below PNIPAM's LCST. Figure 2d shows that free-floating layered bNP film (bNP<sub>200</sub>, dry film thickness  $\sim 2.4$   $\mu\text{m}$ ) exhibited substantial reversible lateral shrinkage at temperatures above PNIPAM's LCST.

Importantly, the specific architecture of bNP–polymer hybrid assemblies (*i.e.*, number of PNIPAM/PMAA bilayers in between bNP) determined anisotropy of their stimuli response (Figure 3). The distinct feature of our work is that previous approaches to light-induced shape changes in polymer gels based on introduction of photosensitive chemical groups<sup>51,52</sup> or on dispersing nanoparticles in a gel matrix<sup>22–25</sup> did not have integrated anisotropic structure and did not provide control of swelling anisotropy. Figure 3a (left)



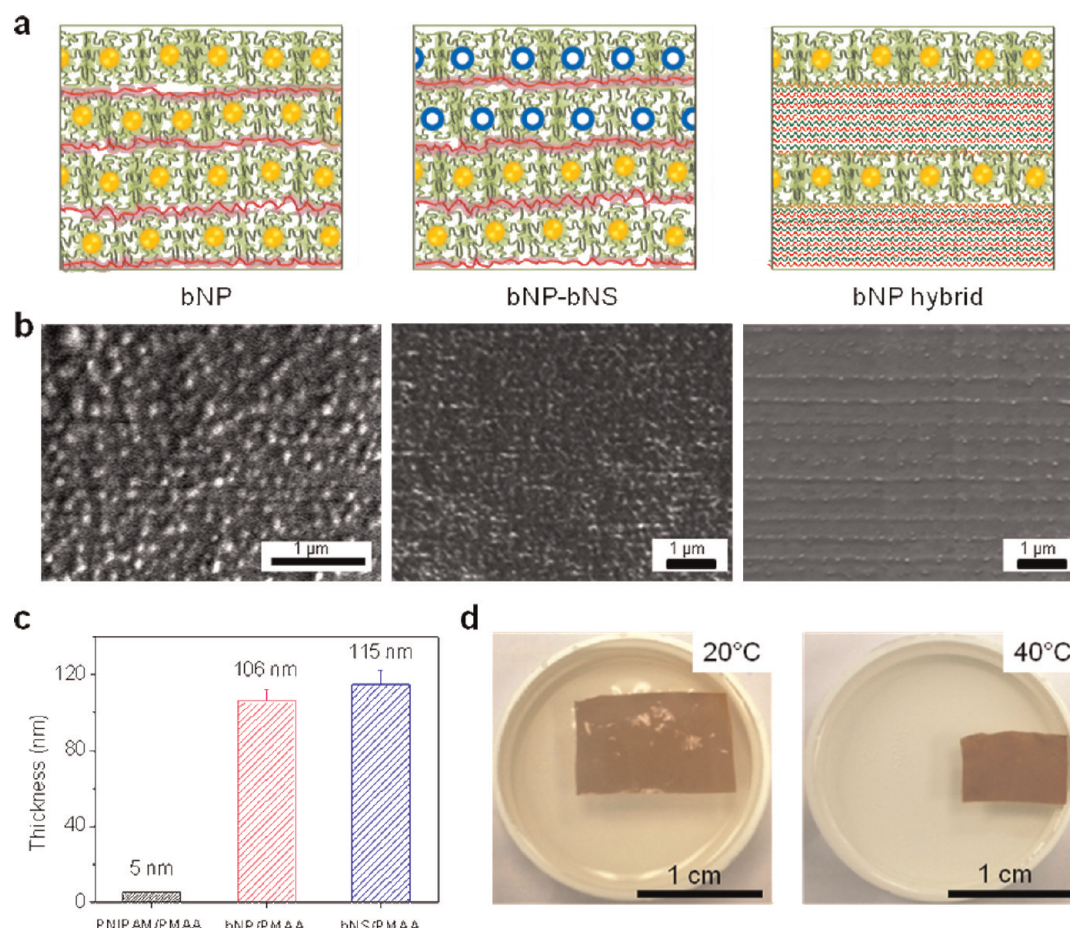


**Figure 2.** Stratified assemblies of polymer-grafted gold nanoparticles and homopolymers. (a) Schematic illustration of layered bNP, bNP–bNS, and bNP–polymer hybrid assemblies. (b) Cross-sectional SEM images of the corresponding spin-coated bNP<sub>500</sub>, bNP<sub>500</sub>–bNS<sub>500</sub>, and (bNP<sub>1</sub>–pol<sub>80</sub>)<sub>30</sub> films. (c) Thicknesses of PNIPAM/PMAA, bNP–PMAA, and bNS–PMAA bilayers as calculated from SEM images. (d) Temperature response of a free-floating bNP<sub>200</sub> film (dry thickness 2.4 μm) in a 0.01 M phosphate buffer solution at pH 3.0.

shows confocal laser scanning microscopy (CLSM) images of cubes microtomed from layered bNP (bNP<sub>1000</sub>) films prewet at 20 °C. Deswelling of microtomed cubes was induced through the photothermal effect. Note that the wavelengths for surface plasmon resonance bands of bNP and bNS after assembly within the multilayer film were not significantly different from those shown in Figure 1d (Figure S6). The absence of plasmonic coupling of metal nanostructures within the film is a result of large spacing between individual plasmonic structures (~300 and ~100 nm distance between metal nanoparticles in bNP assemblies at 20 and 40 °C, respectively) maintained by swellable polymer brushes. Upon illumination of bNP<sub>1000</sub> microcubes with a 546 nm light from a mercury lamp at 75 mW (power density 1.1 W/cm<sup>2</sup>), equilibrium deswelling was reached in ~20 min (Figure 3a, right). Figure S7 shows that kinetics of material deswelling (with bNP assemblies as an example) was dependent on the power of the light source. Control experiments with pure PNIPAM gels showed no effect of incident radiation (performed in the same conditions of illumination as nanoparticle-containing materials) on gel swelling

(Figure S8). bNP assemblies were highly swollen, with swelling ratio  $\lambda = 2.3$  ( $\lambda$  is the ratio of wet to dry linear dimensions), as shown in Figure 3a and c, left, while binding of conformationally unrestricted PNIPAM homopolymer with PMAA generated temperature-insensitive, nonswelling assemblies (Figure 3c, right). This result indicates that PMAA homopolymer did not completely penetrate the PNIPAM brush surrounding bNPs. Comparison of deswelling degrees for the two cases, when bNPs are individually dispersed in solution (Figure 1c) or included within bNP assemblies (Figure 3a and c, left), shows that only ~20% of PNIPAM segments included within the top part of the brush participated in binding with PMAA, while the remaining unbound ~80% maintained temperature response. This estimate was based on the fact that PNIPAM chains lose their ability to swell in aqueous environments after binding with PMAA and that film swelling occurs solely due to the presence of free, PMAA-unbound fraction of polymer units within the brush. Interestingly, bNP assemblies did not have “memory” of a templating surface and swelled isotropically (Figure 3a and c, left) in directions perpendicular and parallel to the substrate

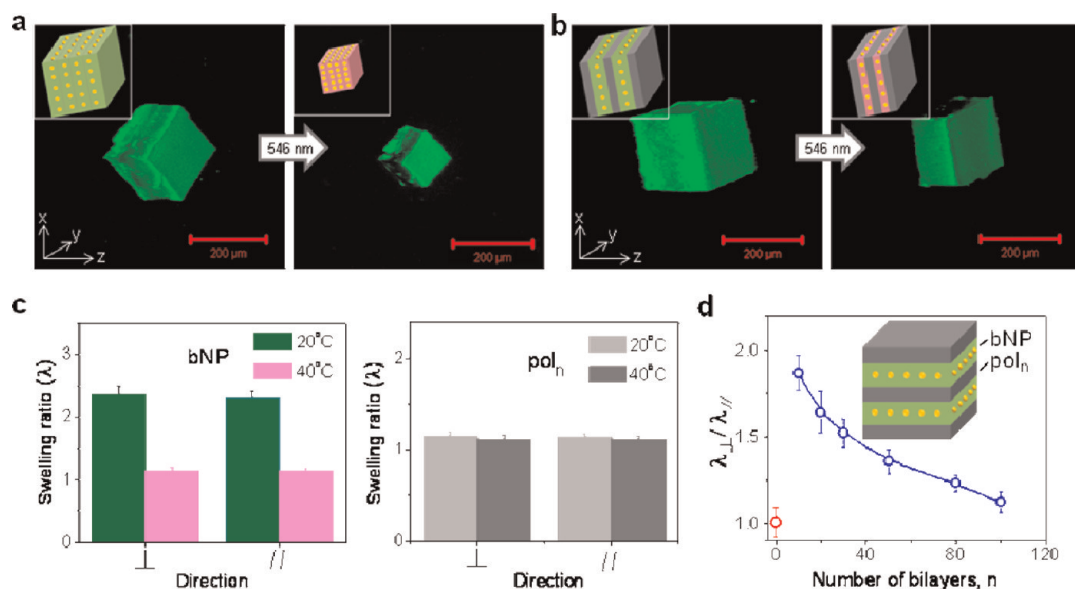


**Figure 3.** Light response of various assemblies of polymer-grafted gold nanoparticles and homopolymers. CLSM 3D images showing light-induced shape changes in bNP (a) and bNP<sub>1</sub>–pol<sub>30</sub> (b) assemblies in aqueous solutions at pH 3.0 after 20 min exposure to 546 nm band-pass-filtered mercury lamp illumination with a power of 75 mW (power density 1.1 W/cm<sup>2</sup>) at the sample. Cubes were microtomed from bNP<sub>1000</sub> and [bNP<sub>1</sub>–pol<sub>30</sub>]<sub>600</sub> films swollen at 20 °C. Solution temperature was maintained at 20 °C during the light exposure. (c) Swelling ratios of bNP and pol (PNIPAM/PMAA) strata in directions perpendicular and parallel to the substrate ( $\lambda_{\perp}$  and  $\lambda_{\parallel}$ , respectively). (d) The effect of  $n$ , *i.e.*, number of pol (PNIPAM/PMAA) bilayers in between bNP layers, in [bNP<sub>1</sub>–pol<sub>n</sub>]<sub>400</sub> assemblies on deswelling anisotropy. The red square ( $n = 0$ ) corresponds to bNP assembly.

(with swelling ratios  $\lambda_{\perp}$  and  $\lambda_{\parallel}$  of 2.3). At the same time, deswelling of bNP–polymer hybrid films was highly anisotropic and occurred exclusively in the direction perpendicular to the film layer plane (Figure 3b). Obviously, in hybrid bNP assemblies changes in in-plane film swelling were suppressed by the binding of bNP particles with nonswelling PNIPAM/PMAA layers. Materials that contract or stretch in a single direction with no changes in dimensions in the other two directions [zero Poisson's ratio (ZPR) materials] can be derived from nature (examples include cork and cornea<sup>53</sup>). However, initial attempts to demonstrate synthetic analogues of such materials are restricted to all-polymer hydrogels under mechanical stimuli.<sup>54</sup> Our bNP–polymer hybrid films are the first example of a ZPR nanocomposite material exhibiting reversible, remotely controlled swelling.

It is important that the degree of anisotropy could be precisely controlled by the spacing between bNP layers (Figure 3d). Inserting 10-bilayer PNIPAM/PMAA spacers with total dry thickness of  $\sim 50$  nm largely restricted material deswelling to the direction perpendicular to the substrate while having only a weak effect on  $\lambda_{\parallel}$  (swelling anisotropy,  $\lambda_{\perp}/\lambda_{\parallel}$  of 1.8). The degree of anisotropy of shape changes in bNP–polymer hybrid assemblies was simply determined by the fractions of responsive bNP and nonresponsive polymer strata in layered assemblies. By increasing the thickness of assembled all-polymer spacer layers,  $\lambda_{\perp}/\lambda_{\parallel}$  could be decreased, reaching a value of 1.1 for the hybrid material with 100-bilayer polymer spacers (in the limit

of infinitely thick polymer spacer layers,  $\lambda_{\perp}/\lambda_{\parallel}$  should approach unity). Figure S9 compares the anisotropic swelling behavior of hybrid bNP–polymer materials for two cases, when cubes were microtomed from films prewet at 20 °C (Figure S9a) or from the dry state (Figure S9b). For both cases, swelling/deswelling ratios and swelling anisotropies were identical, while the variations of the material shape were predetermined by the cutting conditions (wet vs dry).

Hybrid assemblies contain layers of two materials of different elasticity and, therefore, present an interesting case for investigating the mechanical properties of these composites as they go through swelling transition. Multilayer nanocomposites usually exhibit high tensile strength due to binding and stiffening of polymer chains within layers, as well as due to the presence of inorganic components. Earlier work on layered nanocomposites showed elastic moduli of  $\sim 10$  GPa,<sup>55–59</sup> all measured in tensile testing. Our study presents, for the first time, dynamic linear rheological properties of LbL composites in their swollen state. We conducted temperature sweep experiments to characterize the viscoelastic properties of bNP, bNP–pol hybrid assemblies and 2% PNIPAM gels using a strain-controlled rheometer (see Supporting Information and Figures S10 and S11 for details). Storage moduli of bNP and bNP hybrids display a similar transition in a temperature range of 32–36 °C and reached a plateau above 36 °C (Figure 4a). The loss tangent data provide additional insight into anisotropic shrinkage of the hybrid assemblies. Hybrid films

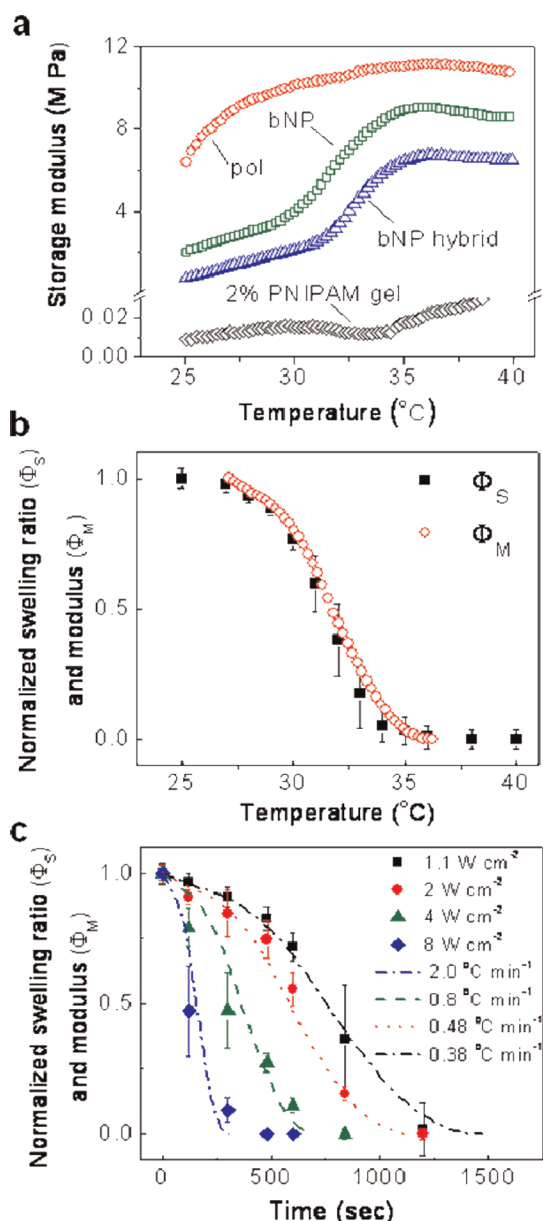


**Figure 4.** Mechanical properties of polymer-grafted gold nanoparticle assemblies as a function of temperature. (a) Viscoelastic measurements for bNP<sub>1000</sub>, pol<sub>5000</sub>, and [bNP<sub>1</sub>–pol<sub>30</sub>]<sub>500</sub> hybrid films. (b) Comparison of CLSM data on temperature-triggered changes in swelling ratios of bNP assembly (cubes cut from bNP<sub>1000</sub> films) with normalized modulus of bNP<sub>1000</sub> films obtained from rheology. (c) Equilibrium swelling of cubes obtained from light-triggered deswelling (points) cut from bNP<sub>1000</sub> films and their corresponding normalized moduli (lines) as a function of time.

show a sharp loss tangent peak attributed to the presence of nonresponsive PNIPAM/PMAA layers, where they transmit the mechanical stresses onto brushes in the z-direction, and show less elastic behavior as compared to bNP assemblies (Figure S11).

We then evaluated the swelling response of bNP assemblies using temperature sweep oscillatory experiments. Figure 4b compares the normalized equilibrated swelling ratios ( $\Phi_S = (S(T) - S_{dry}) / (S_{swollen} - S_{dry})$ ) of bNP assemblies inferred from CLSM with the

normalized elastic modulus ( $\Phi_M = (G'_{dry} - G'(T)) / (G'_{dry} - G'_{swollen})$ ) of the corresponding states. The rate of deformation ( $k_d$ ) is found to be  $0.002 \text{ s}^{-1}$  using the relationship  $k_d = \gamma\omega$ , where  $\gamma$  is the strain amplitude (0.2%),  $\omega$  is the frequency (1 rad/s), and the heat transfer rate  $k_h$  is on the order of  $10^7 \text{ s}^{-1}$  (see Supporting Information). Since  $k_d$  is much lower than the rate of heating, we conclude that samples were in thermal equilibrium during deformation. Rheology data are then used to estimate the swelling rate ( $k_s$ ) by fitting the normalized modulus data to an exponential decay function,  $\Phi_M = \exp(-k_s t)$ .<sup>60</sup> The value of  $k_s$  of  $0.003 \text{ s}^{-1}$  was very close to the rate of deformation ( $k_d$ :  $0.002 \text{ s}^{-1}$ ). Thus, rheology measurements were conducted in a quasi-equilibrium state in the limit of  $k_d/k_s \approx 1$ , when the swelling ratio can be assumed unchanged at any instant of deformation. Swelling ratios at various power intensities and corresponding elastic moduli superimpose when linear shift factors of  $0.38$ – $2.0 \text{ °C/min}$  are applied to the temperature (Figure 4c). This result shows that, at incident light power densities in the range  $1.1$ – $8.0 \text{ W/cm}^2$  mostly used in this work, swelling and elastic response are closely related, and shape changes in swollen bNP assemblies reach their equilibrium shapes. We then projected that a model of heat conduction around a spherical heating source can describe temperature distribution within a collapsed PNIPAM brush. We obtained the temperature distribution around a nanoparticle with a moving boundary condition at the brush surface limited by heat convection (see Supporting Information and Figure S12). While this classical conduction model does not capture the complexity of heat transfer in a collapsing gel at the molecular level, it allows us to predict the following values consistent with experimental results (Figure S11): (1) the end-point thickness of the collapsed brush (determined by reaching the LCST) of 60 nm or higher at power densities  $> 1 \text{ W/cm}^2$  and (2) the threshold power density for the brush collapse of  $0.7 \text{ W/cm}^2$ , in agreement with no deswelling of bNP assemblies detected at  $0.5 \text{ W/cm}^2$ .

Unlike most shape-changing stiff nanocomposites with elastic modulus in the GPa range, our shape-changing materials are significantly softer (elastic modulus in the MPa range, potentially matching human soft tissue) and allow further remote tuning of their mechanical properties by light, a feature making such materials suitable for potential biomedical applications, such as controlling cell and tissue adhesion and/or manipulation of soft tissues. In addition to their attractive light-controlled mechanomutable properties, these materials can additionally control delivery of functional molecules. Figure 5 shows that light-induced deswelling can be used to control diffusion of pyrene molecules entrapped within bNP assemblies at  $20 \text{ °C}$  ( $6.5 \pm 0.2 \text{ mg}$  of pyrene per  $\text{cm}^3$  of bNP



composite). The pyrene release rate to the surrounding solution was strongly enhanced upon irradiation and could be further tuned by the illumination power intensity.

Next, we assembled materials with additional wavelength selectivity to the incident radiation. This was demonstrated by inclusion of two different types of nanoparticles (*i.e.*, bNP and bNS) within separate assembly strata. These assemblies were able to respond

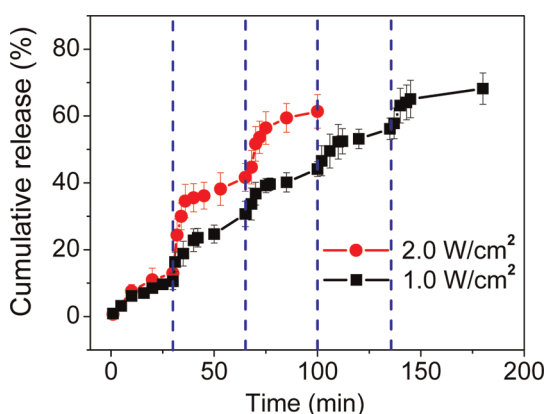


**Figure 5.** Light-controlled on–off release of pyrene from a bNP<sub>1000</sub> film (wet thickness 0.25 mm at 20 °C) at different power densities of light. Pyrene-loaded bNP<sub>1000</sub> films were immersed in a pH 3.0 buffer at 20 °C, and the samples were exposed to several on–off cycles of illumination, consisting of exposure to a 532 nm laser for a period of 5 min, followed by turning off the laser while keeping the sample in the water bath at 20 °C for 30 min.

to wavelength radiation resonant to either NPs or NSs through deswelling that occurred into spatially resolved material layers. Double-strata bNP–bNS films were able to bend in response to irradiation at 785 or 532 nm (Figure 6). Unlike previous reported cases when bending always occurred in the direction of laser illumination (such as with liquid-crystalline materials containing photoresponsive functional groups),<sup>7,8</sup> our layered films allow for controlling the bending direction through the film nanostructure, independently of the irradiation direction (Figure 6). This was due to the transparency of the bNP and bNS in 785 or 532 nm spectral regions, respectively (see Figure 1d).

Selectivity of the layered material's response was further demonstrated by CLSM, when cubes were microtomed from either two- or three-strata films (bNP–bNS, Figure 7a–c, and bNS–bNP–bNS, Figure 7d–f, respectively). Shown in Figure 7 are equilibrated shapes, observed after the hydrogels reached the end-point deswelling states under 1.1 W/cm<sup>2</sup> 546 nm or 2 W/cm<sup>2</sup> 785 nm light irradiation. Figure S13 illustrates that deswelling of the central layer can be selectively achieved under continuous resonant irradiation with a moderate-intensity light at 1.1 W/cm<sup>2</sup>, whereas at increased illumination power of 4 W/cm<sup>2</sup>, nonabsorbing film strata can also collapse due to enhanced heat transfer. Importantly, all shape changes were highly reversible in the thermally and light-driven response for more than three cycles. Microcubes in Figure 3 a, b and Figure 7, whose shape changes

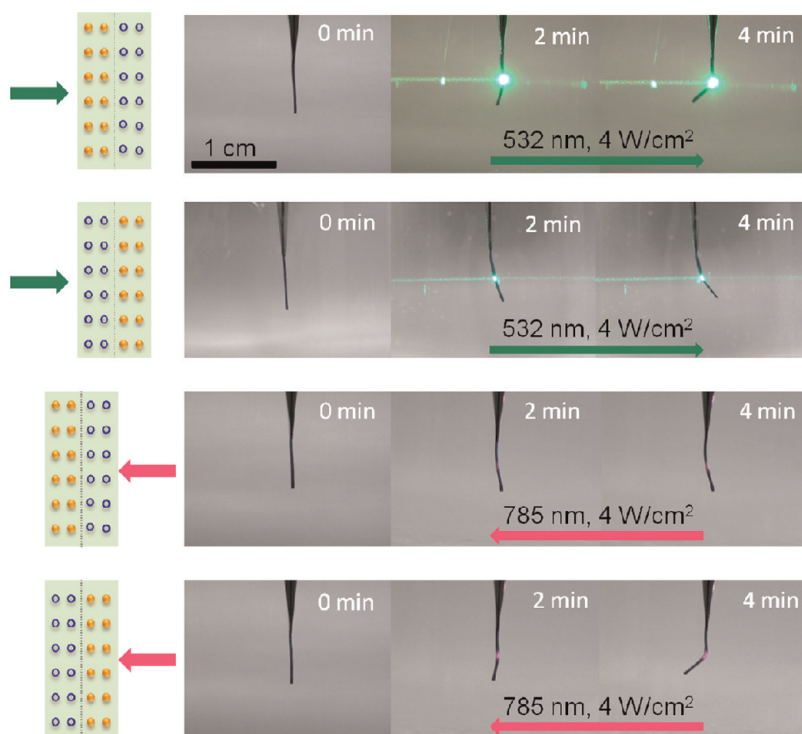


**Figure 6.** Wavelength- and nanostructure-controlled bending of bNP–bNS films. bNP<sub>500</sub>–bNS<sub>500</sub> films of ~220 μm thickness were immersed in pH 3 0.01 M phosphate buffer solution at 20 °C under laser irradiation at two different wavelengths. Arrows indicate the direction of light application.



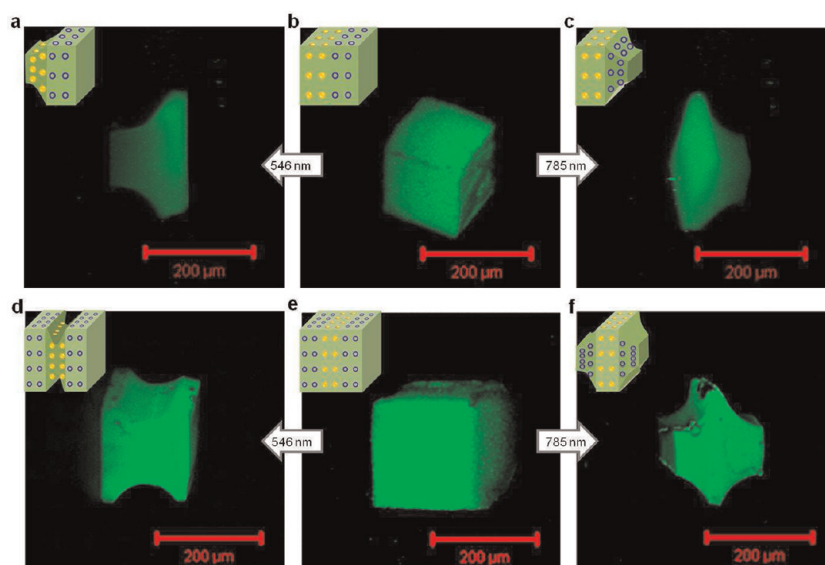


**Figure 7.** Wavelength-selective shape changes in stratified assemblies of polymer-grafted gold nanoparticles and nanoshells. (a–c) CLSM images of light-controlled shape changes in two-strata  $\text{bNP}_{500}$ – $\text{bNS}_{500}$  cubes upon irradiation using wavelengths at 546 nm ( $1.1 \text{ W/cm}^2$ ) and 785 nm ( $2 \text{ W/cm}^2$ ). (d–f) Similar experiments with three-strata  $\text{bNS}_{300}$ – $\text{bNP}_{400}$ – $\text{bNS}_{300}$  cubes. Illumination time was 20 min.

reached equilibrium after 15 min, recovered their original state within  $\sim 5 \text{ s}$  after the laser was turned off.

## CONCLUSION

In summary, here we present a novel approach to designing light-responsive soft materials that exhibit diverse, nanostructure-encoded, reversible shape changes. Precise localization of brush-decorated nanostructures within the film enabled controlling the anisotropy of material swelling and yielded the first ZPR materials allowing remotely controlled unidirectional changes in swelling. Importantly, a broad range of shape variations at specific wavelengths can be realized with these layered nanocomposites through independent variation of metal nanoparticle type, thicknesses of nonresponsive and responsive layers, and various combinations of nanoparticles. Specifically, by changing gold nanostructure shape and size and/or by exploring different chemistries of metal

cores, a variety of polymer–metal building blocks absorbing light within a broad spectral range from UV/visible to near-infrared can be synthesized. At the same time, the application of LbL technique to precisely control the spacing between these responsive nanostructures, as well as to regulate the anisotropy of material swelling, will potentially generate a range of wavelength-specific geometric variations with these materials. These assemblies present exciting new possibilities for using light to realize multiple functionalities in nanostructured materials, including remote dynamic control of nanocomposite mechanical properties, shape, and the ability to retain small molecules. These features are useful in mimicking functions of complex biological tissues, as well as in nanoengineering novel materials for interfacing biology. The approach is versatile and can be extended to a broad range of “soft” nanoparticles with built-in responsiveness.

## METHODS

**Materials.** *N*-Isopropylacrylamide (Aldrich, 97%) was purified twice by recrystallization from a mixture of hexane and benzene (7/3, v/v). 2-(Dimethylamino)ethyl methacrylate (Aldrich, 98%) was distilled twice under reduced pressure to remove inhibitors. *N,N*-Dimethylformamide (DMF) (Aldrich, 99%) was freshly distilled under reduced pressure before use. The disulfide initiator  $[\text{S}-(\text{CH}_2)_{11}-\text{OCOC}(\text{CH}_3)_2\text{Br}]_2$  was synthesized according to the literature<sup>61</sup> and characterized by  $^1\text{H}$  NMR spectroscopy. Millipore (Milli-Q system) water with a  $18.2 \text{ M}\Omega \text{ cm}^{-1}$  resistivity was used. PNIPAM and PMAA with  $M_w$  150k and 300k, respectively, were purchased from Scientific Polymer Products Inc. Branched polyethylenimine (BPEI) with  $M_w$  25k, *N,N,N',N',N'*-penta-methyldiethylenetriamine (PMDETA), CuBr,  $\text{HAuCl}_4$ , hydrochloric acid, sodium hydroxide, sodium chloride, and dibasic and monobasic sodium phosphate were purchased from Sigma-

Aldrich. All other reagents were purchased from Sigma-Aldrich and used as received. All glassware was treated with a potassium dichromate/sulfuric acid mixture and thoroughly rinsed with tap and deionized water prior to use.

**Synthesis of Metal Cores and bNP and bNS Particles.** NPs with  $70 \pm 10 \text{ nm}$  diameter and NSs with  $65 \pm 6 \text{ nm}$  external diameter and  $\sim 4 \text{ nm}$  shell thickness (Figure S1) were synthesized according to literature procedures.<sup>38,39</sup> Thermosensitive polymer brushes were “grafted from” NPs and NSs by ATRP with a procedure similar to that described elsewhere<sup>62</sup> using the CuBr/PMDETA complex as the catalyst system. The initiator-modified gold NPs or NSs were prepared from citrate-stabilized gold nanoparticles through ligand exchange between the disulfide initiator and citrates in DMF. Typically, 50 mg of  $[\text{S}-(\text{CH}_2)_{11}-\text{OCOC}(\text{CH}_3)_2\text{Br}]_2$  was dissolved in 200 mL of DMF, and then 200 mL of an aqueous solution containing 200 mg of NP (or 40 mg of NSs) was added

dropwise during 6 h. The mixture was vigorously stirred for 12 h, and excess initiator was removed by centrifugation. Initiator-capped gold nanoparticles were dispersed in DMF. The capping density of the ATRP initiator was determined by TGA (data not shown) as about 1830 and 2100 ligands per particle for bNPs and bNSs, respectively. For "grafting from" a copolymer of NIPAM and DMA, NIPAM (2.0 g), DMA (40 mg), initiator-capped nanoparticles (100 mg of NPs or 20 mg of NSs), CuBr (6 mg), and DMF/H<sub>2</sub>O (5 mL, 7:3, v/v) were added to a round-bottom flask, and the mixture was degassed by three freeze–pump–thaw cycles under argon. A degassed mixture of PMDETA (18 mg) dissolved in 1.0 mL of DMF was injected into the flask with gentle stirring. After 12 h of polymerization, the system was opened to air for 30 min to terminate the reaction. Finally, the bNPs or bNSs were separated by centrifugation and washed with 2-propanol and water. To determine copolymer compositions and molecular weights, copolymer brushes were detached from the gold surface by iodine treatment as described previously.<sup>40</sup> The resultant copolymer materials were washed by deionized water and dried under vacuum.

**Multilayer Assembly.** Silicon wafers were cleaned as described elsewhere.<sup>63</sup> To enhance surface adhesion of subsequently grown multilayers, the substrate was coated with a BPEI/PMAA bilayer as a precursor layer, deposited from 0.2 mg/mL solutions 0.01 M in phosphate buffer at pH 5.5. Substrates with deposited BPEI/PMAA precursor film were rinsed in Milli-Q water and used for construction of multilayer films.

Multilayer films were assembled on treated substrate with spin-assisted LbL technique using a 0.5 mg/mL solution of bNP or bNS and 0.2 mg/mL solutions of PNIPAM and PMAA in 0.01 M phosphate buffer at pH 3. Substrate rotation speed was 3000 rpm, and deposition time was 10 s per layer, with the applications of two buffer rinsing solutions for 10 s each.

**Characterization of Nanostructures.** Molecular weights, molecular weight distributions, and chemical composition of grafted copolymer chains were determined after polymer chains were cleaved from NPs or NSs. In GPC analysis, GPC Styragel columns HT3 and HT4 maintained at a temperature of 35 °C and a Waters 2414 differential refractive index detector (set at 30 °C) were used. DMF was used at a flow rate of 1.0 mL/min. Chromatographic columns have been calibrated with standard polystyrene samples. Copolymer composition was determined by <sup>1</sup>H NMR in D<sub>2</sub>O at room temperature using a Varian Inova 400 MHz NMR spectrometer. TGA of bNP and bNS particles was performed with samples placed in aluminum pans using a Polymer Laboratories TG1000 instrument operating in the 20–650 °C temperature range, under nitrogen, at a heating rate of 20 °C/min.

TEM images were measured using a FEI CM20 field emission microscope with an operating voltage of 200 kV. For TEM imaging, samples were dispersed in H<sub>2</sub>O and deposited on carbon-coated copper grids. SEM was performed using a Zeiss Auriga dual-beam FIB-SEM. To prepare SEM samples, dry films were cut with a razor blade in the direction perpendicular to the film surface. Cross sections were then irradiated with a 2 keV electron beam for ~10 s to develop clear and smooth morphology for imaging. The particle size and size distribution were measured by dynamic light scattering using Zetasizer Nano-ZS equipment from Malvern Instruments, Ltd. UV–vis spectra were recorded on a Perkin-Elmer Lambda 35 UV–vis spectrophotometer using a 1 cm wide glass cuvette. Contact mode AFM experiments were performed using a NSCRIPTOR dip pen nanolithography system (Nanoink) using P-MAN-SICT-0 AFM cantilevers (PacifiC Nanotechnology, Inc.) with a nominal force constant of 0.2 N/m. The polymer-modified bNPs were suspended in H<sub>2</sub>O (5 µg/mL), and a drop of the suspension was deposited onto the precursor-coated silicon wafer surface at a controlled temperature of 20 or 40 °C.

**Light Sources.** For studies of photothermally driven size changes of films and microcubes, as well as dye release of nanocomposite assemblies, the following light sources were used: (a) CLSM-mounted mercury lamp at 546 nm (75 mW, power density 1.1 W/cm<sup>2</sup>), (b) external DPSS 532 nm continuous radiation diode pumped solid-state laser (Laserglow Technologies) with a beam diameter of 2 mm, or (c) a

fiber-coupled PI-ECL-785-300-SMA laser of wavelength 785 nm (Process Instruments, Inc.) with a fiber core diameter of 0.6 mm. The power density at the samples was controlled with the help of filter sets. The external laser sources were switched off during CLSM imaging to avoid the effects of scattered radiation.

**Dye Loading and Release.** To achieve loading, substrate-deposited bNP multilayers were immersed in saturated 0.68 µM pyrene aqueous solutions at pH 3.0 at 20 °C under stirring for 5 h. The films were then taken out of solution and immersed in a fresh buffer for 10 min at 20 °C to remove free pyrene. To determine the loading content of pyrene within the films, 1 cm × 1 cm silicon wafers covered with pyrene-loaded films were immersed in 10 mL of acetone solution to achieve extraction of loaded pyrene. The pyrene extract was then analyzed with fluorescence spectroscopy using excitation at 338 nm and emission at 391 nm, and the amount of pyrene included within multilayers was calculated from a calibration curve obtained with acetone solutions of free pyrene with known concentrations.

To trigger pyrene release, bNP<sub>n</sub> films immersed in solutions at 20 °C were illuminated with a 532 nm laser with the power density 1 and 2 W/cm<sup>2</sup>. Briefly, light-triggered release of pyrene from the bNP<sub>n</sub> films was performed by immersing pyrene-loaded films in a beaker containing 20 mL of pH 3.0 buffer at 20 °C using a water bath, followed by an exposure of the sample to 1 W/cm<sup>2</sup> 532 nm laser at 20 °C for a period of 5 min and then turning off the laser while keeping the sample in the water bath at 20 °C for 30 min. The procedure was repeated for several cycles between "on" and "off" states of the 532 nm laser. Aliquots (0.5 mL) were removed from the buffer solution every 5 min, quickly analyzed by fluorometry, and injected back into the buffer media. The concentration of released pyrene in the samples was calculated based on the standard curve obtained with pyrene solutions in pH 3.0 buffer.

In all cases, cumulative release (%) expressed as the total percentage of pyrene released was calculated as  $W_t/W \times 100$ , where  $W_t$  is the cumulative weight of dye released by time  $t$  and  $W$  is the total weight of dye loaded.

**Preparation of Free-Standing Films and Microcubes.** To release films from solid substrates, multilayers were immersed in 0.01 M phosphate buffer solutions at pH 3.0 and repetitively heated/cooled to 40 °C/20 °C, keeping films at each temperature for 10 min. After several temperature cycles, multilayers delaminated from the substrate.

Microcubes were cut from free-standing multilayers using a homemade sled microtome with the range of the cut thicknesses between 100 and 200 µm. The thickness of multilayer films of 100–200 µm was determined by optical microscopy and was set as the cut thickness. Multilayers were then sequentially cut with a knife blade in two mutually perpendicular directions, which were normal to the original substrate used in film assembly.

**Confocal Laser Scanning Microscopy Imaging of Films and Microcubes.** Confocal images were obtained using an LSM 5 PASCAL laser scanning microscope (Zeiss, Germany) equipped with a Plan-NeoFluar 10×/0.3 objective. Prior to imaging, microcubes were treated with Alexa-488 dye according to the procedure recommended by the supplier. In brief, a drop of dispersed microcubes was transferred to 20 µg of an Alexa-488 pH 3.0 solution for 2 h at room temperature. Unretained dye was then removed by five cycles of washing (2 min per cycle) with 5 mL of buffer solution at pH 3.0. A drop of a dispersion of precut microcubes was added to a homemade, temperature-controlled 12-well holder with stainless steel walls and 170 µm thick coverglass bottom and diluted with buffer solutions at pH 3.0 to ~1 mL. Microcubes were allowed to settle for 20 min prior to imaging.

**Rheology Measurements.** Viscoelastic properties were measured using an ARES-G2 (TA Instruments) rheometer with stainless steel 8 mm parallel plate geometry. A layer of waterproof sandpaper (3M) with a grid size of 220 was glued on both plates in order to prevent slipping of the plates on the sample surfaces. Samples were cut larger than 8 mm to ensure that sample fills the gap when it shrinks at LCST. Supplementary Figure 5 shows that the sample diameter did not have an effect

on measured values of moduli. All experiments were performed in a forced convection oven maintaining the temperature within  $\pm 0.1$  °C. After 3 min equilibration at 25 °C, sinusoidal strain with an amplitude of 0.2% (in the linear region) was applied to the samples at an angular frequency of 1 rad/s in the oscillation-temperature ramp mode. The temperature was increased from 25 °C to 40 °C at the rate of 1 °C/min. The torque values were recorded with a 1 Hz sampling rate, and the corresponding  $G'$  ( $\omega$ ) (storage) and  $G''$  ( $\omega$ ) (viscous) moduli were obtained. In order to prevent detachment of the samples from the geometry due to changes in thicknesses, a normal force of 3 N was maintained throughout the measurements (excluding the initial equilibration time), and the gap between the plates was adjusted accordingly.

**Conflict of Interest:** The authors declare no competing financial interest.

**Acknowledgment.** The research leading to these results has received partial support from the NSF under grant DMR-0906474. E.S. and P.A. acknowledge support from the Stevens Institute of Technology startup fund. This research effort used microscope resources partially funded by the National Science Foundation through NSF grant DMR-0922522.

**Supporting Information Available:** TEM images of NPs and NSs; TGA data for bNP and bNSs; GPC and  $^1\text{H}$  NMR characterization of grafted chains; SEM images of bNP-containing films; deswelling kinetics of bNP assemblies; PNIPAM gel under irradiation; shape changes in bNP-pol hydrid films cut from a wet film; spatially resolved shape changes in triple-stratum bNS–bNP–bNS assemblies, as well as further detailed description of sweep experiments and the heat transfer model. This material is available free of charge via the Internet at <http://pubs.acs.org>.

## REFERENCES AND NOTES

- Stuart, M. A. C.; Huck, W. T. S.; Genzer, J.; Müller, M.; Ober, C.; Stamm, M.; Sukhorukov, G. B.; Szleifer, I.; Tsukruk, V. V.; Urban, M. Emerging Applications of Stimuli-Responsive Polymeric Materials. *Nat. Mater.* **2010**, *9*, 101–113.
- Sun, T.; Qing, G. Biomimetic Smart Interface Materials for Biological Applications. *Adv. Mater.* **2011**, *23*, H57–H77.
- Ionov, L.; Houbenov, N.; Sidorenko, A.; Stamm, M.; Minko, S. Stimuli-Responsive Command Polymersurface for Generation of Protein Gradients. *Biointerphases* **2009**, *4*, FA45–FA49.
- Ebara, M.; Aoyagi, T.; Kikuchi, A.; Sakai, K.; Okano, T. Temperature-Responsive Cell Culture Surfaces Enable “on-off” Affinity Control between Cell Integrins and RGDS Ligands. *Biomacromolecules* **2004**, *5*, 505–510.
- Abu-Lail, N. I.; Kaholek, M.; LaMattina, B.; Clark, R. L.; Zauscher, S. Micro-Cantilevers with End-Grafted Stimulus-Responsive Polymer Brushes for Actuation and Sensing. *Sens. Actuators B* **2006**, *114*, 371–378.
- Liu, Z. S.; Calvert, P. Multilayer Hydrogels as Muscle-Like Actuators. *Adv. Mater.* **2000**, *12*, 288–291.
- Yu, Y. L.; Nakano, M.; Ikeda, T. Directed Bending of a Polymer Film by Light—Miniaturizing a Simple Photomechanical System Could Expand Its Range of Applications. *Nature* **2003**, *425*, 145–145.
- Ikeda, T.; Nakano, M.; Yu, Y.; Tsutsumi, O.; Kanazawa, A. Anisotropic Bending and Unbending Behavior of Azobenzene Liquid-Crystalline Gels by Light Exposure. *Adv. Mater.* **2003**, *15*, 201–205.
- Van Oosten, C. L.; Bastiaansen, C. W. M.; Broer, D. J. Printed Artificial Cilia from Liquid-Crystal Network Actuators Modularly Driven by Light. *Nat. Mater.* **2009**, *8*, 677–682.
- Koerner, H.; Price, G.; Pearce, N. A.; Alexander, M.; Vaia, R. A. Remotely Actuated Polymer Nanocomposites—Stress-Recovery of Carbon-Nanotube-Filled Thermoplastic Elastomers. *Nat. Mater.* **2004**, *3*, 115–120.
- Ahir, S. V.; Terentjev, E. M. Photomechanical Actuation in Polymer–Nanotube Composites. *Nat. Mater.* **2005**, *4*, 491–495.
- Fava, D.; Winnik, M. A.; Kumacheva, E. Photothermally-Triggered Self-Assembly of Gold Nanorods. *Chem. Commun.* **2009**, *18*, 2571–2573.
- Von Maltzahn, G.; Park, J.-H.; Agrawal, A.; Bandaru, N. K.; Das, S. K.; Sailor, M. J.; Bhatia, S. N. Computationally Guided Photothermal Tumor Therapy Using Long-Circulating Gold Nanorod Antennas. *Cancer Res.* **2009**, *69*, 3892–3900.
- Yavuz, M. S.; Cheng, Y.; Chen, J.; Cobley, C. M.; Zhang, Q.; Rycenga, M.; Xie, J.; Kim, C. H.; Song, K. H.; Schwartz, A. G. Gold Nanocages Covered by Smart Polymers for Controlled Release with Near-Infrared Light. *Nat. Mater.* **2009**, *8*, 935–939.
- Poon, L.; Zandberg, W.; Hsiao, D.; Erno, Z.; Sen, D.; Gates, B. D.; Branda, N. R. Photothermal Release of Single-Stranded DNA from the Surface of Gold Nanoparticles Through Controlled Denaturing and Au–S Bond Breaking. *ACS Nano* **2010**, *4*, 6395–6403.
- Timko, B. P.; Dvir, T.; Kohane, D. S. Remotely Triggerable Drug Delivery Systems. *Adv. Mater.* **2010**, *22*, 4925–4943.
- Sershen, S. R.; Mensing, G. A.; Ng, M.; Halas, N. J.; Beebe, D. J.; West, J. L. Independent Optical Control of Microfluidic Valves Formed from Optomechanically Responsive Nanocomposite Hydrogels. *Adv. Mater.* **2005**, *17*, 1366–1368.
- Lee, S. E.; Liu, G. L.; Kim, F.; Lee, L. P. Remote Optical Switch for Localized and Selective Control of Gene Interference. *Nano Lett.* **2009**, *9*, 562–570.
- Huschka, R.; Neumann, O.; Barhoumi, A.; Halas, N. J. Visualizing Light-Triggered Release of Molecules inside Living Cells. *Nano Lett.* **2010**, *10*, 4117–4122.
- Sershen, S. R.; Westcott, S. L.; Halas, N. J.; West, J. L. Independent Optically Addressable Nanoparticle-Polymer Optomechanical Composites. *Appl. Phys. Lett.* **2002**, *80*, 4609–4611.
- Sershen, S.; West, J. L. Implantable, Polymeric Systems for Modulated Drug Delivery. *Adv. Drug Delivery Rev.* **2002**, *54*, 1225–1235.
- Shiotani, A.; Mori, T.; Niidome, T.; Niidome, Y.; Katayama, Y. Stable Incorporation of Gold Nanorods into N-Isopropylacrylamide Hydrogels and Their Rapid Shrinkage Induced by Near-Infrared Laser Radiation. *Langmuir* **2007**, *23*, 4012–4018.
- Das, M.; Sanson, N.; Fava, D.; Kumacheva, E. Microgels Loaded with Gold Nanorods: Photothermally Triggered Volume Transitions under Physiological Conditions. *Langmuir* **2007**, *23*, 196–201.
- Budhlall, B. M.; Marquez, M.; Velev, O. D. Microwave, Photo- and Thermally Responsive PNIPAm-Gold Nanoparticle Microgels. *Langmuir* **2008**, *24*, 11959–11966.
- Zhang, J.; Xu, S.; Kumacheva, E. Polymer Microgel: Reactors for Semiconductor, Metal and Magnetic Nanoparticles. *J. Am. Chem. Soc.* **2004**, *126*, 7908–7914.
- Decher, G. Fuzzy Nanoassemblies: Toward Layered Polymeric Multicomposites. *Science* **1997**, *277*, 1232–1237.
- Wang, T. C.; Cohen, R. E.; Rubner, M. F. Metallo-dielectric Photonic Structures Based on Polyelectrolyte Multilayers. *Adv. Mater.* **2002**, *14*, 1534–1537.
- Caruso, F.; Caruso, R. A.; Möhwald, H. Nanoengineering of Inorganic and Hybrid Hollow Spheres by Colloidal Templating. *Science* **1998**, *282*, 1111–1114.
- Sukhorukov, G.; Fery, A.; Möhwald, H. Intelligent Micro- and Nanocapsules. *Prog. Polym. Sci.* **2005**, *30*, 885–897.
- Birnkrant, M. J.; Li, C. Y.; Natarajan, L. V.; Tondiglia, V. P.; Sutherland, R. L.; Lloyd, P. F.; Bunning, T. J. Layer-in-Layer Hierarchical Nanostructures Fabricated by Combining Holographic Polymerization and Block Copolymer Self-Assembly. *Nano Lett.* **2007**, *7*, 3128–3133.
- Kulkarni, D. D.; Choi, I.; Singamaneni, S. S.; Tsukruk, V. V. Graphene Oxide-Polyelectrolyte Nanomembranes. *ACS Nano* **2010**, *4*, 4667–4676.
- Li, D.; Cui, Y.; Wang, K.; He, Q.; Yan, X.; Li, J. Thermosensitive Nanostructures Comprising Gold Nanoparticles Grafted with Block Copolymers. *Adv. Funct. Mater.* **2007**, *17*, 3134–3140.
- Kim, D. J.; Kang, S. M.; Kong, B.; Kim, W.-J.; Paik, H.-J.; Choi, H.; Choi, I. S. Formation of Thermoresponsive Gold Nanoparticle/PNIPAAm Hybrids by Surface-Initiated, Atom Transfer Radical Polymerization in Aqueous Media. *Macromol. Chem. Phys.* **2005**, *206*, 1941–1946.

34. Svetushkina, E.; Pureskiy, N.; Ionov, L.; Stamm, M.; Synytska, A. Comparative Study on Switchable Adhesion Between Thermoresponsive Polymer Brushes on Flat and Rough Surfaces. *Soft Matter* **2011**, *7*, 5691–5696.
35. Radt, B.; Smith, T. A.; Caruso, F. Optically Addressable Nanostructured Capsules. *Adv. Mater.* **2004**, *16*, 2184–2189.
36. Bédard, M. F.; De Geest, B. G.; Skirtach, A. G.; Möhwald, H.; Sukhorukov, G. Remote Release from Polyelectrolyte Microcapsules. *Adv. Colloid Interface Sci.* **2010**, *158*, 2–14.
37. Radziuk, D.; Shchukin, D. G.; Skirtach, A.; Möhwald, H.; Sukhorukov, G. Synthesis of Silver Nanoparticles for Remote Opening of Polyelectrolyte Microcapsules. *Langmuir* **2007**, *23*, 4612–4617.
38. Jana, N. R.; Gearheart, L.; Murphy, C. J. Seeding Growth for Size Control of 5–40 nm Diameter Gold Nanoparticles. *Langmuir* **2001**, *17*, 6782–6786.
39. Schwartzberg, A. M.; Olson, T. Y.; Talley, C. E.; Zhang, J. Z. Synthesis, Characterization, and Tunable Optical Properties of Hollow Gold Nanospheres. *J. Phys. Chem. B* **2006**, *110*, 19935–19944.
40. Kim, J.-B.; Huang, W.; Bruening, M. L.; Baker, G. L. Synthesis of Triblock Copolymer Brushes by Surface-Initiated Atom Transfer Radical Polymerization. *Macromolecules* **2002**, *35*, 5410–5416.
41. Fujishige, S.; Kubota, K.; Ando, I. Phase Transition of Aqueous Solutions of Poly(*N*-isopropylacrylamide) and Poly(*N*-isopropylmethacrylamide). *J. Phys. Chem.* **1989**, *93*, 3311–3313.
42. Winnik, F. M. Fluorescence Studies of Aqueous Solutions of Poly(*N*-isopropylacrylamide) below and above Their LCST. *Macromolecules* **1990**, *23*, 233–242.
43. Laloyaux, X.; Mathy, B.; Nysten, B.; Jonas, A. M. Surface and Bulk Collapse Transitions of Thermoresponsive Polymer Brushes. *Langmuir* **2010**, *26*, 838–847.
44. Xu, L.; Zhu, Z.; Borisov, O.; Zhulina, E.; Sukhishvili, S. A. pH-Triggered Block Copolymer Micelle-to-Micelle Phase Transition. *Phys. Rev. Lett.* **2009**, *103*, 118301.
45. Kreibitz, U.; Vollmer, M. *Optical Properties of Metal Clusters*; Springer: Berlin, 1995; p 25.
46. Cho, J.; Char, K.; Hong, J. D.; Lee, K. B. Fabrication of Highly Ordered Multilayer Films Using a Spin Self-Assembly Method. *Adv. Mater.* **2001**, *13*, 1076–1078.
47. Chiarelli, P. A.; Johal, M. S.; Casson, J. L.; Roberts, J. B.; Robinson, J. M.; Wang, H.-L. Controlled Fabrication of Polyelectrolyte Multilayer Thin Films using Spin-Assembly. *Adv. Mater.* **2001**, *13*, 1167–1171.
48. Jiang, C.; Markutsya, S.; Tsukruk, V. V. Collective and Individual Plasmon Resonances in Nanoparticle Films Obtained by Spin-Assisted Layer-by-Layer Assembly. *Langmuir* **2004**, *20*, 882–890.
49. Kharlampieva, E.; Sukhishvili, S. A. Hydrogen-Bonded Layer-by-Layer Polymer Films. *J. Macromol. Sci., Part C, Polym. Rev.* **2006**, *46*, 377–395.
50. Jiang, C.; Tsukruk, V. V. Free Standing Nanostructures via Layer-by-Layer Assembly. *Adv. Mater.* **2006**, *18*, 829–840.
51. Suzuki, A.; Tanaka, T. Phase Transition in Polymer Gels Induced by Visible Light. *Nature* **1990**, *346*, 345–347.
52. Mamada, A.; Tanaka, T.; Kungwachakun, D.; Irie, M. Photo-induced Phase Transition of Gels. *Macromolecules* **1990**, *23*, 1517–1519.
53. Matsuura, T.; Ikeda, H.; Idota, N.; Motokawa, R.; Hara, Y.; Annaka, M. Anisotropic Swelling Behavior of the Cornea. *J. Phys. Chem. B* **2009**, *113*, 16314–16322.
54. Haque, M. A.; Kamita, G.; Kurokawa, T.; Tsujii, K.; Gong, J. P. Unidirectional Alignment of Lamellar Bilayer in Hydrogel: Anisotropic Swelling, Anisotropic Modulus, and Stress/Strain Tunable Structural Color. *Adv. Mater.* **2010**, *22*, 5110–5114.
55. Podsiadlo, P.; Kaushik, A. K.; Arruda, E. M.; Waas, A. M.; Shim, B. S.; Xu, J.; Nandivada, H.; Pumphlin, B. G.; Lahann, J.; Ramamoorthy, A. Ultrastrong and Stiff Layered Polymer Nanocomposites. *Science* **2007**, *318*, 80–83.
56. Podsiadlo, P.; Tang, Z.; Shim, B. S.; Kotov, N. A. Counterintuitive Effect of Molecular Strength and Role of Molecular Rigidity on Mechanical Properties of Layer-by-Layer Assembled Nanocomposites. *Nano Lett.* **2007**, *7*, 1224–1231.
57. Wang, J.; Cheng, Q.; Tang, Z. Layered Nanocomposites Inspired by the Structure and Mechanical Properties of Nacre. *Chem. Soc. Rev.* **2012**, *41*, 1111–1129.
58. Podsiadlo, P.; Arruda, E. M.; Kheng, E.; Waas, A. M.; Lee, J.; Critchley, K.; Qin, M.; Chuang, E.; Kaushik, A. K.; Kim, H. S. LBL Assembled Laminates with Hierarchical Organization from Nano- to Microscale: High-Toughness Nanomaterials and Deformation Imaging. *ACS Nano* **2009**, *3*, 1564–1572.
59. Patro, T. U.; Wagner, H. D. Layer-by-Layer Assembled PVA/Laponite Multilayer Free-Standing Films and their Mechanical and Thermal Properties. *Nanotechnology* **2011**, *2*, 455706.
60. Tanaka, T.; Fillmore, D. J. Kinetics of Swelling of Gels. *J. Chem. Phys.* **1979**, *70*, 1214–1218.
61. Shah, R. R.; Mercey, D.; Husemann, M.; Rees, I.; Abbott, N. L.; Hawker, C. J.; Hedrick, J. L. Using Atom Transfer Radical Polymerization To Amplify Monolayers of Initiators Patterned by Microcontact Printing into Polymer Brushes for Pattern Transfer. *Macromolecules* **2000**, *33*, 597–605.
62. Li, D.; He, Q.; Cui, Y.; Li, J. Fabrication of pH-Responsive Nanocomposites of Gold Nanoparticles/Poly(4-vinylpyridine). *Chem. Mater.* **2007**, *19*, 412–417.
63. Kozlovskaya, V.; Yakovlev, S.; Libera, M.; Sukhishvili, S. Surface Priming and the Self-Assembly of Hydrogen-Bonded Multilayer Capsules and Films. *Macromolecules* **2005**, *38*, 4828–4836.